The Meteoritical Society

Meteoritics & Planetary Science 52, Nr 12, 2550–2569 (2017)
doi: 10.1111/maps.12954

Coordinated EDX and micro-Raman analysis of presolar silicon carbide: A novel, nondestructive method to identify rare subgroup SiC

Nan LIU[1*], Andrew STEELE[2], Larry R. NITTLER[1], Rhonda M. STROUD[3], Bradley T. De Gregorio[3], Conel M. O'D. ALEXANDER[1], and Jianhua WANG[1]

[1]Department of Terrestrial Magnetism, Carnegie Institution for Science, Washington, DC 20015, USA
[2]Geophysical Laboratory, Carnegie Institution for Science, Washington, DC 20015, USA
[3]Materials Science and Technology Division, Code 6366, US Naval Research Laboratory, Washington, DC 20375–5320, USA
[*]Corresponding author. E-mail: nliu@carnegiescience.edu

(Received 29 November 2016; revision accepted 05 August 2017)

Abstract–We report the development of a novel method to nondestructively identify presolar silicon carbide (SiC) grains with high initial $^{26}Al/^{27}Al$ ratios (>0.01) and extreme ^{13}C-enrichments ($^{12}C/^{13}C \leq 10$) by backscattered electron-energy dispersive X-ray (EDX) and micro-Raman analyses. Our survey of a large number of presolar SiC demonstrates that (1) ~80% of core-collapse supernova and putative nova SiC can be identified by quantitative EDX and Raman analyses with >70% confidence; (2) ~90% of presolar SiC are predominantly 3C-SiC, as indicated by their Raman transverse optical (TO) peak position and width; (3) presolar 3C-SiC with $^{12}C/^{13}C \leq 10$ show lower Raman TO phonon frequencies compared to mainstream 3C-SiC. The downward shifted phonon frequencies of the ^{13}C-enriched SiC with concomitant peak broadening are a natural consequence of isotope substitution. ^{13}C-enriched SiC can therefore be identified by micro-Raman analysis; (4) larger shifts in the Raman TO peak position and width indicate deviations from the ideal 3C structure, including rare polytypes. Coordinated transmission electron microscopy analysis of one X and one mainstream SiC grain found them to be of 6H and 15R polytypes, respectively; (5) our correlated Raman and NanoSIMS study of mainstream SiC shows that high nitrogen content is a dominant factor in causing mainstream SiC Raman peak broadening without significant peak shifts; and (6) we found that the SiC condensation conditions in different stellar sites are astonishingly similar, except for X grains, which often condensed more rapidly and at higher atmospheric densities and temperatures, resulting in a higher fraction of grains with much downward shifted and broadened Raman TO peaks.

INTRODUCTION

A variety of grain types in primitive meteorites have been confirmed as presolar stardust grains based on their highly anomalous isotopic compositions, including carbon-rich phases (diamond, graphite, silicon carbide [SiC], graphene, and TiC), oxygen-rich phases (corundum, spinel, hibonite, TiO_2, and silicates), and silicon nitride (Anders and Zinner 1993; Zinner et al. 2003). In particular, SiC is the most extensively studied presolar phase because of its rarity in the solar system, relatively large size (~μm), and resistance to acid dissolution. These properties make it relatively easy to isolate candidate presolar SiC from meteorites via acid treatments. Isotopic analysis is the traditional way to verify presolar SiC grains, which show anomalous isotopic compositions of carbon, nitrogen, silicon, noble gases, and a number of heavy elements (e.g., strontium, zirconium, and barium), relative to the solar system and Earth (e.g., Zinner et al. 1987; Nicolussi et al. 1997, 1998a, 1998b; Lugaro et al. 2003; Savina et al. 2003, 2004; Heck et al. 2007).

The classification of presolar SiC grain subgroups is mainly based on their C-, N-, and Si-isotopic ratios, which can be measured by secondary ion mass

[Correction added on 11 October 2017, after first online publication: In the first column on Page 7, "simultaneously collecting $^{12}C_2^-$, $^{12}C^{13}C^-$, $^{14}N_2^-$, $^{14}N^{15}N^-$, $^{28}Si^-$, $^{29}Si^-$, and $^{30}Si^-$" was changed to "simultaneously collecting $^{12}C_2^-$, $^{12}C^{13}C^-$, $^{12}C^{14}N^-$, $^{12}C^{15}N^-$, $^{28}Si^-$, $^{29}Si^-$, and $^{30}Si^-$".]

spectrometry (SIMS). Presolar SiC grains have been divided into a number of subgroups, including mainstream, Y, Z, AB, so-called putative nova grains (PNGs), X, C1, and C2 (Alexander 1993; Nittler et al. 1996; Hoppe et al. 1997; Amari et al. 2001a, 2001b; Liu et al. 2016). In detail, the dominant population, mainstream grains (~90%), is inferred to have originated in outflows from low-mass asymptotic giant branch (AGB) stars with close-to-solar metallicities. They have $^{12}C/^{13}C$ ratios between 10 and 100, a wide range of $^{14}N/^{15}N$ ratios, and slightly ^{28}Si-poor silicon. Relative to mainstream grains, types Y and Z grains (on the order of 1% for each type) came from lower metallicity AGB stars, based on the observations that type Z grains are more enriched in ^{30}Si and type Y grains have $^{12}C/^{13}C$ ratios higher than 100 (e.g., Zinner 2014). In addition, types X (1–2%), C1 (0.1%), and C2 (<0.1%) grains have diverse isotope signatures pointing toward an origin in the ejecta of core-collapse supernovae (CCSNe), with their varied isotopic compositions indicating heterogeneous mixing processes during CCSN explosions (e.g., Liu et al. 2016). For instance, X and C1 grains have similar carbon isotopic ratios ($^{12}C/^{13}C > 10$) and excesses in ^{15}N, but X grains are enriched in ^{28}Si, while C1 grains show excesses in both ^{29}Si and ^{30}Si, indicating that the C1 grains originated from more external layers of CCSNe than the X grains. In contrast, C1 and C2 grains both show similar excesses in ^{29}Si and ^{30}Si, but C2 grains have $^{12}C/^{13}C$ ratios lower than 10, indicating that, unlike C1 grains, they formed in regions of their parent CCSNe that experienced explosive hydrogen burning. Similar to C2 grains, PNGs are highly enriched in both ^{13}C and ^{15}N, but show larger excesses in ^{30}Si relative to ^{29}Si; both CCSNe and novae are their potential stellar sources. Finally, although AB grains (~5%) are also characterized by $^{12}C/^{13}C$ ratios lower than 10, they have a wide range of $^{14}N/^{15}N$ ratios (from 20 to 10,000) and silicon isotopic compositions similar to those of mainstream grains. Silicon isotopes can be used to distinguish ^{15}N-enriched AB grains from PNGs and C2 grains (e.g., Amari et al. 2001b). Recent studies of AB grains found that ^{15}N-rich AB ($^{14}N/^{15}N \leq 440$, the solar ratio, AB1 grains) and ^{14}N-rich AB grains ($^{14}N/^{15}N > 440$, AB2 grains) show systematic differences in their light- and heavy-element isotopic compositions with AB1 grains sourced from CCSNe with explosive H burning and AB2 grains mainly from J-type carbon stars (Liu et al. 2017a, 2017b).

Although much has been learned about mixing and nucleosynthetic processes in low-mass AGB stars through multielement isotopic and microstructural studies of mainstream SiC grains since their discovery 30 yr ago (Daulton et al. 2002, 2003; Zinner et al. 2006, 2007; Liu et al. 2014a, 2014b, 2015), similar detailed analyses of other isotopic subgroups of presolar SiC grains (rare subgroup SiC hereafter) are still quite limited mainly because of their rarity and generally smaller sizes relative to mainstream grains. Identification of rare subgroup SiC usually requires SIMS isotopic analyses of a large number of grains. Currently, these searches are most commonly carried out with Cameca NanoSIMS 50/50L instruments that have a spatial resolution on the order of 100 nm when using the Cs^+ ion source for carbon, nitrogen, and silicon isotope analyses. Development of automated SIMS particle analysis methods has greatly sped up searches for rare subgroup SiC grains (Gyngard et al. 2010; Hoppe et al. 2010). However, there are fewer than 10 available NanoSIMS instruments that are dedicated to cosmochemical studies around the world, and none are solely dedicated to presolar grain work. NanoSIMS instrument time is therefore quite limited and expensive. More importantly, SIMS analysis is destructive and implants Cs^+ into the surface of a sample, which could result in changes in surface crystallinity, loss of noble gases, and isobaric interferences for barium isotope analysis (Savina et al. 2003; Heck et al. 2015). Thus, it is highly desirable to develop inexpensive, rapid, and nondestructive methods to identify rare subgroup presolar SiC grains based on alternative characteristics, which will eventually allow for structural and isotopic studies of such grains in institutions that do not have access to the NanoSIMS.

In principle, CCSN grains can be identified by the characteristic magnesium peak in their energy dispersive X-ray (EDX) spectra acquired in a scanning electron microscope (SEM). Magnesium is not expected to condense into SiC during condensation, but aluminum is. Thus, aluminum is one of the most abundant trace elements (up to several wt%) in presolar SiC grains, while the abundance of magnesium (prior to ^{26}Al decay to ^{26}Mg, $\tau_{1/2} = 0.72$ Ma) is more than two orders of magnitude lower (i.e., $^{27}Al/^{24}Mg > 100$; Groopman et al. 2015; Liu et al. 2016). The expectation is that almost all magnesium in SiC grains comes from the decay of ^{26}Al. This is supported by the fact that no anomalous $^{25}Mg/^{24}Mg$ ratios have been reported for presolar SiC grains, even in X grains, although CCSN models predict tens of thousands of permil enrichments in $\delta^{25}Mg/^{24}Mg$. Given the fact that presolar SiC grains from CCSNe show extremely high initial $^{26}Al/^{27}Al$ ratios (~0.01–1), types X, C1, and C2 grains should be characterized by higher-than-average magnesium abundances because of the contribution to radiogenic ^{26}Mg from ^{26}Al decay. Although a few studies have reported the finding of significant magnesium peaks in the EDX spectra of X grains (Hynes et al. 2010; Lin

et al. 2010), there has not been a systematic and detailed study to investigate the reliability and applicability of magnesium abundance measurements for identifying X, C1, and C2 grains.

Silicon carbide is also a particularly interesting mineral phase because it exists in about 250 crystalline polytypes. The formation of these polytypes depends strongly on the growth conditions (e.g., temperature, pressure, gas composition, and substrate), and under common laboratory conditions, 4H, 6H, and 15R are the most easily synthesized polytypes. However, when Daulton et al. (2003) used transmission electron microscopy (TEM) to study the microstructures of ~500 presolar SiC grains with a median diameter of 400 nm in an acid residue of the Murchison meteorite, they found that cubic SiC (3C-SiC) was the dominant polytype (~80%). The only other common structures they observed for presolar SiC were 2H, intergrowths of 3C and 2H, and a few one-dimensionally stacking disordered grains. Daulton et al. (2002, 2003) studied these grains as drop-cast onto carbon support films through a combination of electron diffraction and high-resolution lattice imaging, when permitted by sample thickness constraints. Recently, microtome and focused ion beam (FIB) lift-out techniques have been used to prepare TEM thin sections of presolar SiC grains for TEM studies (Stroud et al. 2004, 2015; Hynes et al. 2010; Kodolányi et al. 2016), but the former results in fragmentation of SiC grains and the latter is time-consuming. Thus, there have been only a few TEM studies of presolar SiC thin sections so far.

In addition to TEM, Raman spectroscopy can be a powerful technique for distinguishing different SiC polytype structures (table 2 of Nakashima and Harima 1997; Nakashima et al. 1986). For instance, Wopenka et al. (2010) previously reported a noncubic SiC Raman spectrum for an atypically large (~30 μm) X grain (grain LU-13, also known as "Bonanza"; Zinner et al. 2011). More recently, Ivanov et al. (2014) showed that the Raman band positions of synthetic isotope-enriched SiC are shifted with respect to those of the same polytype but with normal (i.e., terrestrial) isotopic ratios. As the carbon, nitrogen, and silicon isotopic compositions of presolar SiC grains vary by up to several orders of magnitude, it is an intriguing possibility that there are detectable systematic shifts of Raman band positions due to isotopic substitution in presolar SiC grains. Any such shifts could potentially provide a novel, rapid, and nondestructive method to find rare subgroup SiC grains with extremely anomalous isotopic ratios. Thus, Raman measurements of individual presolar SiC grains have the possibility, in some cases, to simultaneously constrain both the type of star and ambient conditions (pressure, temperature, etc.) that gave rise to the grain, which until now has required both SIMS and TEM observations. We report here Raman spectroscopy data that distinguish the population of mainstream SiC grains with 3C structure from those of the same polytype but with large ^{13}C enrichments indicative of formation in non-AGB circumstellar environments (Liu et al. 2016, 2017a, 2017b). We furthermore demonstrate that supernova and ^{13}C-enriched SiC grains can be reliably and efficiently identified by their higher-than-average radiogenic magnesium concentrations and lower shifted Raman peaks, respectively, using SEM and Raman spectroscopy. Finally, we show that targeting the grains with highly shifted and broadened transverse optical (TO) peak positions for TEM analysis is an effective way to identify grains of the rarer polytypes, e.g., 6H and 15R.

EXPERIMENTAL METHODS

Sample Description and Preparation

The SiC grains in this study were extracted from a ~63 g sample of the Murchison CM2 meteorite by following the CsF-based isolation method described by Nittler and Alexander (2003). A density separation was first conducted based on the density difference between the CsF solution (~1.5 g/cc) and the insoluble organic matter (IOM) with the remaining unattacked minerals. A small fraction (~1/63) of the total IOM was used to extract SiC grains. After destruction of the IOM, a crude size separation was conducted based on settling times in water to reduce the number of small grains. The extracted SiC grains range from 0.5 to 2 μm with a median size of 0.9 μm. A small fraction of the total SiC residue was dispersed onto a high-purity gold foil attached onto an aluminum stub, and was subsequently pressed into the gold with an optically flat sapphire disk. Two sample mounts were prepared, referred to here as mounts #1 and #2. We also obtained optical images of the two mounts at ×20 magnification, which were automatically stitched together to generate maps with the Nikon Element software to guide subsequent microanalyses using different techniques.

Automated BSE-EDX Analysis

A JEOL 6500F field emission SEM equipped with an Oxford Instruments silicon drift detector (SDD, Oxford X-max 80) was used for the backscattered electron (BSE)-EDX analyses of presolar SiC grains. Because the atomic mass of gold is much larger than that of SiC and other mineral phases, such as spinel, that are typically found in the residues, most of the

mineral grains appeared as black dots on the bright substrate in each BSE image. The operating voltage was set at 10 kV to increase the spatial resolution relative to a typical working voltage of 15 kV, at a working distance of 10 mm, and with a beam current of ~1 nA. The analyzed volume can be approximated by a sphere of about 1 μm^3 for each EDX spectrum. The Oxford EDX system software (AZtec) includes both stage automation and the recently developed AZtec Feature software that allow for automatic particle analysis. Automated BSE-EDX particle analysis is a common technique for gunshot residue analysis, and was used by Choi et al. (1998) to help identify presolar oxide grains in meteorites.

In this study, the automated measurements consisted of the following sequence. A 150 × 150 μm^2 BSE image was first acquired at a resolution of 30 nm px^{-1}. With the particle definition software in AZtec, individual grains were identified by their intensity in each BSE image according to defined criteria. The grains were then individually measured by electrostatically deflecting the electron beam to their centers and acquiring EDX spectra for 30−60 s. After analysis of each selected grain in a given BSE image, the sample stage was moved and the entire process was repeated. The intensity threshold for grain identification was set by choosing the "magic button" in the Feature toolbox and clicking on a known grain in a BSE image. The appropriate threshold was established with this grain and applied to all the BSE images during an automated mapping. We set the minimum equivalent circle diameter (ECD) for identifying grains at 0.7 μm (25 pixels); a maximum ECD value cannot be defined in the software. With this automated BSE-EDX system, potentially thousands of grains can be automatically analyzed over the course of a day without user intervention.

Automated grain analysis can also be conducted with the NanoSIMS (Gyngard et al. 2010; Hoppe et al. 2010) but at much lower rates. Given the analytical conditions used in the Gyngard et al. study, the BSE-EDX automated analysis is made much faster by the fact that (1) no Cs^+ presputtering is required (~100 min for each 150 × 150 μm^2 area in NanoSIMS) and (2) each 1024 × 1024 BSE image can be acquired in 10 s, much faster than ion image acquisition (~300 min for each 150 × 150 μm^2 area in NanoSIMS). Even assuming the same acquisition time for each grain analysis, it would take more than 4 months to scan a 3 × 3 mm area with the automated NanoSIMS analysis compared to 2 weeks using the automated BSE-EDX system. Direct ion imaging searches in Cameca ims-series ion microprobes can identify X grains faster than automated NanoSIMS grain analyses (Nittler et al. 1996; Hoppe et al. 2000), but is still destructive and substantially slower than the BSE-EDX method. Thus, if the quantitative magnesium abundance obtained by EDX analysis of presolar SiC grains can be used to identify X grains, the automated BSE-EDX analysis is clearly a much faster tool for rapidly locating X grains. This is especially true for mounts made with low grain densities to avoid clumping of grains that can lead to mixing of isotopic anomalies and consequently misleading constraints on the origins of the grains as well as nucleosynthesis and mixing in their parent stars.

The EDX spectra acquired here were quantified by means of standards with the AZtec software. For the EDX analysis, pyrope (a type of garnet) was used as the standard for silicon and oxygen and ENAL20 (enstatite aluminum 20 wt%, an aluminum-bearing enstatite glass) for magnesium and aluminum. Both standards are well polished and have been used for X-ray analysis at Carnegie for a long time. We also analyzed a suite of other pure elemental and oxide standards for normalizing the grain data, and the relative differences in the derived carbon, oxygen, magnesium, aluminum, and silicon abundances are within 10%. Thus, the EDX results of our study are not significantly affected by the choice of standards. More importantly, as we are mainly interested in the differences of the minor element concentrations between mainstream and rare subgroup SiC grains in this study, such small systematic errors caused by the matrix difference between the standards and the samples will not affect any of our conclusions.

As the SiC grains are pressed into gold in this study, the gold M-line peak at 2.2 keV is present in all the EDX spectra. This peak was excluded, i.e., fixed at 0 wt%, during data reduction by using the MiniQuant function in AZtec software. Moreover, hydrocarbon contamination is quite common on our grain mounts, as indicated by our SiC grain analyses often showing higher-than-unity carbon to silicon atomic ratios. Thus, in order to minimize the effect of carbon contamination on EDX results, we fixed the silicon concentration to its nominal value in stoichiometric SiC of 70 wt% in the AZtec software to quantify the concentrations of carbon, oxygen, magnesium, and aluminum. The EDX data errors are calculated by considering 1σ statistical uncertainties in MiniQuant; other uncertainties such as peak fit errors are not included, and thus the reported errors only represent lower limits. The mean 2σ uncertainty in the magnesium concentration is 0.06 wt% for 70 SiC grains that had detectable magnesium contents (i.e., higher than 2σ errors), and these 70 SiC grains were subsequently analyzed for isotopic compositions of carbon, nitrogen, and silicon with the NanoSIMS for classification. The EDX and NanoSIMS data are summarized in Table S1 in supporting information.

Micro-Raman Analysis

Confocal Raman Microscope

Raman signals of SiC can be easily obtained if the fluorescence background is kept low, as the Raman efficiency of SiC is high because of the strong covalent Si-C bond. We used a WITeC multifunction scanning probe microscope to acquire Raman spectra on 156 single and well-isolated presolar SiC grains. This instrument includes near-field optical microscopy and confocal Raman imaging microscopy. A 532 nm frequency-doubled Nd:YAG laser was used for SiC grain measurements that has a typical spatial resolution of ~400 nm at low power. The Raman microscope is equipped with two automated stages: an X-Y linear stage for ~10 mm motion in each direction with a 1 μm reproducibility, and a piezo-driven X-Y linear stage for <200 μm motion in each direction with ~2 nm reproducibility. The first step was to acquire a Raman spectral image for each grain with an acquisition time of 2 s px^{-1} at a spatial resolution of 370 nm px^{-1}, where each pixel contains a full Raman spectrum (~0.1Δ cm^{-1} spectral resolution in the range 0−3700 cm^{-1}). The Raman images were quite noisy due to the relatively short acquisition times and were mainly used to center on the grains. Then by clicking on each Raman image using the mouse, the stage automatically moved to the pixel that has the maximum Raman signal. An average spectrum of 5–10 single Raman measurements on each grain was then collected with 10 s acquisition time per spectrum to maximize the signal-to-noise ratio. For grains with interesting Raman features, we also imaged the grains with longer acquisition times, 10−20 s px^{-1}, to increase the signal-to-noise ratios, enabling investigation of internal crystal structural heterogeneities.

Heating Effect of Laser Power

All the Raman spectra reported here were acquired with less than 20 mW laser intensity. The primary Raman spectral feature for SiC is the TO phonon peak at ~760−800 cm^{-1}. Bauer et al. (2009) quantified the effect of laser power on the TO phonon frequency shift to be ~0.005 cm^{-1} mW^{-1} for both 6H-SiC and 4H-SiC using a Raman system similar to the one in our study. The laser power used in our study therefore corresponds to less than a 0.1 cm^{-1} shift in the frequency. We also tested the heating effect of laser power on presolar SiC Raman features and found that the power needs to be increased by at least a factor of 10 before the TO peak starts to show a systematic downward shift of 1−2 cm^{-1}, which is in good agreement with the Bauer et al. (2009) results. It is noteworthy to point out that the small heating effect of laser power on the SiC Raman signal is mainly the result of the small absorption coefficient of SiC at 532 nm so that only a very small fraction of the laser energy is absorbed in the material. For comparison, the heating effect on silicon is almost an order of magnitude larger, 0.03 cm^{-1} mW^{-1}, at this wavelength (Bauer et al. 2009). We chose single and well-isolated SiC grains identified by high-resolution SEM and NanoSIMS ion images for Raman analysis to avoid signal interferences from adjacent grains, and succeeded in obtaining high signal-to-noise Raman spectra on 149 single SiC grains in the size range of 0.7–2.0 μm. The Raman signals of the other seven SiC grains are below the detection limit. The Raman data are summarized in Table S2 in supporting information.

Raman Spectrometer Calibration

Although the Raman microscope itself is equipped with an internal neon lamp to calibrate the multichannel Raman spectrometer, the peak at 0 cm^{-1} that results from the reflected laser beam is shifted by varying amounts in Raman spectra that were taken at different times. We, therefore, monitored the long-term stability of the spectrometer to quantify the precision of our Raman measurements by using an external argon–mercury (Ar-Hg) lamp and also an external neon lamp. We found that although the measured Raman peak positions of all the Ar-Hg (~400−1200 cm^{-1}) and neon emission lines (~1700−3600 cm^{-1}) had uncertainties on the order of 0.1 cm^{-1} during runs of 2–3 days, the peak positions were shifted relative to the reference values by varying amounts over a period of several months. In addition, the fact that the Ar-Hg and neon lines in different spectral regions are shifted by varying amounts clearly demonstrates that the offsets are not caused by variations in the laser beam wavelength, which should result in a constant shift over the whole spectral region from 0 to 3600 cm^{-1}. Instead, the observed nonlinear line shifts indicate that there are inaccuracies associated with the internal calibration method in the WITeC software.

We thus recalibrated the multichannel spectrometer using the external Ar-Hg and neon lamp spectral data collected in our study (Fig. 1). For a grating spectrometer, in principle, wavelength should vary linearly with pixel number. However, as previously noticed by Tseng et al. (1993), a linear fit usually results in large systematic errors in the calculated line positions, and a quadratic relationship was used in their study to relate wavelength to pixel number in order to significantly reduce the fit residuals. In good agreement with the Tseng et al. (1993) results, our Ar-Hg and neon line data also show that a linear fit results in a large fit residual and that a quadratic relationship with the pixel number gives a much better fit to the data

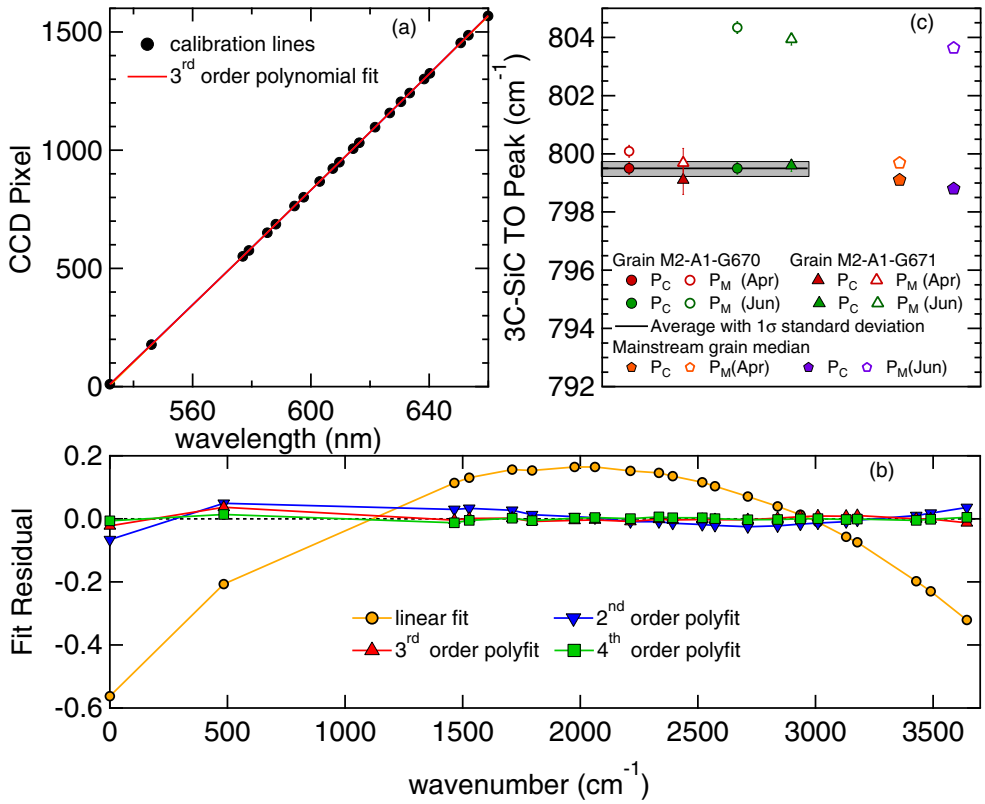

Fig. 1. a) Ar-Hg and neon line data are plotted as CCD pixel versus wavelength, with a third-order polynomial fit to the data. b) Fit residuals of different polynomial fits to the line data are plotted against wavenumber. c) Raman TO peak positions of two single SiC grains measured at two different times are shown for comparison. After calibration, the two measured data points for each grain and also the average Raman peak positions of mainstream SiC grains measured in April (Apr) and June (Jun) 2016 are consistent with each other. Note that in this plot, P_M is measured peak position, and P_C is corrected position. (Color figure can be viewed at wileyonlinelibrary.com.)

(Fig. 1b). To further improve the fit to the grain data, we also tried higher order polynomial fits and found that a third-order polynomial fit results in a further improvement in the accuracy of calibrated line positions in lower wavenumber region, and that the difference between a third-order and a fourth-order polynomial fit is negligible. Thus, we adopted third-order polynomial fits to relate wavelength to pixel number for spectrometer calibration in our study, which is in fact also the standard method for calibrating multichannel detectors recommended by Ocean Optics, Inc. (the manufacturer of the Ar-Hg calibration lamp used in our study). As shown in Fig. 1c, the Raman data for two single SiC grains measured during two different sets of runs in April and June 2016 are in good agreement with a standard deviation of 0.2 cm^{-1} after calibration. Also, we measured a large number of mainstream presolar SiC grains (~30–50 grains each time) during the two sets of runs. The corrected mean TO peak positions of mainstream 3C-SiC grains for both data sets are also consistent with each other within 0.2 cm^{-1} after calibration. Thus, we conclude that the calibration method adopted in our study is quite robust and the resultant uncertainties are within 0.2 cm^{-1}.

We also analyzed a number of terrestrial 6H-SiC grains and hexagonal BN grains (found as contaminants on the sample mounts) as standards during our Raman analyses. On average, the measured Raman peak positions of 6H-SiC and hexagonal BN after calibration are both ~3 cm^{-1} higher than their standard reference values of 789 and 1366 cm^{-1} for 6H-SiC and hexagonal BN, respectively. For the Raman data in Table S2, however, we report the raw measured values, because 6H-SiC and hexagonal BN minerals used in our analyses are not certified standards for structural analysis. More importantly, we are mainly interested in the difference between mainstream and rare subgroup SiC grains, and such a constant offset will not affect any of our conclusions. It is also worth pointing out that the literature Raman data for synthetic and presolar SiC cannot be directly compared with the grain data in our study because of differences in calibration methods, especially given that the calibration methods adopted in the literature studies often were not reported in detail.

The full width at half maximum (FWHM) value, Γ, for the SiC TO Raman peak was calculated by using a Gaussian fitting function. The FWHM of the Raman instrument response function that is related to the sensitivity of the instrument (Fryling et al. 1993) was determined to be 3.6 cm^{-1} based upon Ar-Hg and neon atomic lines. The intrinsic linewidth of a sample was then corrected for the instrumental linewidth using the equation given by Pelletier (1999)

$$\Gamma_{samp} = (\Gamma_{orig}{}^2 - \Gamma_{inst}{}^2)^{0.5} \quad (1)$$

where Γ_{samp} represents the corrected FWHM value of the sample, Γ_{orig} is the measured FWHM value, and Γ_{inst} is the instrumental FWHM value. The uncertainties in the reported Raman peak position and FWHM consider both the standard deviation of Ar-Hg and neon data (0.1–0.2 cm^{-1} during different runs), and the standard deviation of multiple grain measurements (at least two spectra obtained for each grain).

Effects of Electron and Ion Beam Damage

We found that SiC grains that had been analyzed in the SEM prior to Raman analysis all showed D and G bands of amorphous carbon in their subsequent Raman spectra, indicating surface hydrocarbon deposition in the SEM (e.g., M1-A7-G866 in Fig. 2). In contrast, such amorphous carbon peaks were essentially absent in the Raman spectra of SiC grains that were not exposed to any electron beam prior to Raman measurements (e.g., M1-R7 in Fig. 2). In addition, as the Raman data for a few grains reported in Table S2 were collected after NanoSIMS analysis, we also tested the effect of Cs^+ sputtering on the Raman signatures of SiC grains by comparing Raman spectra of five presolar SiC grains that were collected before and after the NanoSIMS analysis (Table S2). We found that there was no measurable TO peak shift resulting from ion beam sputtering for any of the five grains, and that the peak is only slightly broadened by ~1 cm^{-1} (Table S2). The effect of ion beam damage on SiC Raman spectral features is thus negligible under the NanoSIMS analytical conditions of our study.

NanoSIMS Isotope Imaging

Carbon, nitrogen, and silicon isotopic compositions of SiC grains measured with Raman spectroscopy and with detectable magnesium in their EDX spectra were subsequently measured with the Carnegie NanoSIMS 50L ion microprobe, by using a Cs^+ primary ion beam (~1 pA, ~100 nm) and simultaneously collecting $^{12}C_2^-$, $^{12}C^{13}C^-$, $^{12}C^{14}N^-$, $^{12}C^{15}N^-$, $^{28}Si^-$, $^{29}Si^-$, and $^{30}Si^-$ secondary ions with 1–2 min acquisition times. Note that 12 SiC grains were not measured for their nitrogen isotopes due to a problem with a NanoSIMS detector in one set of the runs. In total, 70 SiC grains had measurable magnesium contents (>2σ errors) in the EDX analysis and 156 SiC grains, including 32 of the 70 ones with measurable magnesium, were measured with the Raman microscope. Isotope data were therefore obtained for 194 SiC grains. The isotope data were collected in the NanoSIMS imaging mode to monitor the distribution of potential carbon and nitrogen contamination, and also allow for subsequent comparison with corresponding EDX and Raman images. The analytical conditions for NanoSIMS isotope analyses have been described in Liu et al. (2016) in detail. The carbon and nitrogen isotopic data are given as absolute atomic ratios, and silicon isotopic data in δ notation in the unit of permil (‰) with 1σ errors in Tables S1 and S2.

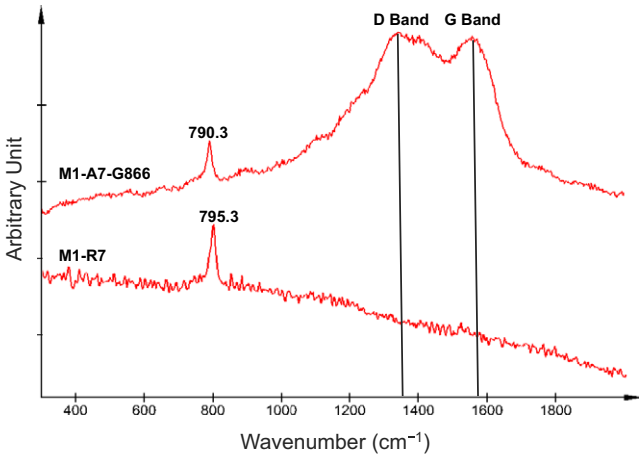

Fig. 2. Raman spectra of mainstream SiC grain M1-R7 prior to BSE-EDX analysis and of AB grain M1-A7-G866 after BSE-EDX analysis. (Color figure can be viewed at wileyonlinelibrary.com.)

Focused Ion Beam and Transmission Electron Microscopy

Grains with Raman spectra suggestive of non-3C polytypes were targeted for structural analysis with TEM. Electron transparent sections of grains M1-A8-G26, M2-A1-G706, and M1-A7-G878 were extracted with FIB lift-out. The grains were protected with either carbon or platinum masks that were deposited in the Nova 600 FIB-SEM at the Naval Research Laboratory (NRL) and the Zeiss Auriga Crossbeam FIB-SEM at Carnegie Institution, respectively. Sections were extracted, attached to copper Omniprobe™ grids, and thinned to ~100 nm. A range of scanning transmission

electron microscopy (STEM) measurements were performed on the sections, including bright field (BF), high-angle annular-dark field (HAADF) imaging, and EDX, with the Nion UltraSTEM-200X and attached windowless Bruker SDD at NRL. The operating conditions were 200 keV with a ~100 pA, 0.2 nm probe. Selected area electron diffraction patterns (SAEDPs) and corresponding goniometer tilts were recorded with the JEOL 2200FS field emission TEM at NRL, equipped with a Gatan OneView camera and GMS3 software. The 2200FS was operated at 200 keV. The camera constants for diffraction measurements were calibrated with a polycrystalline aluminum diffraction standard, and experimental patterns were recorded at the same reference conditions (camera length, sample Z height, and convergence) to provide an instrumental uncertainty of <2%. The SiC SAEDPs were measured with the Calidris CRISP software, and searched against the reference structure polytypes 3C, 2H, 4H, 6H, 8H, 15R, 21R, and 33R with PhIDO. For confidence in the indexing, three-zone axis patterns and their relative angles were matched for each grain. Experimental patterns were also compared with simulated patterns.

RESULTS

Carbon, Nitrogen, and Silicon Isotopic Data

The NanoSIMS isotopic data of the 194 single presolar SiC grains are shown in Fig. 3. The samples include 124 mainstream, 32 X, 22 AB, 8 Y, 3 Z grains, 4 PNGs, as well as 1 ungrouped grain. The isotopic data are in good agreement with the literature data. For instance, the mainstream SiC grains lie along a best-fit line with a slope of 1.59 ± 0.19, consistent with that reported in Zinner et al. (2007). All the isotopes were collected in the imaging mode so that we were able to select small regions of interest for isotopic ratio calculations to avoid surface carbon and nitrogen contamination.

Coordinated BSE-EDX and NanoSIMS Data

In total, we scanned ~3 × 3 mm areas on mounts #1 and #2 in the SEM and identified ~2000 SiC grains (this number should be considered as a lower limit due to grain aggregation on the sample mounts) from 0.7 to 3 μm across with a median diameter of 0.9 μm. According to their EDX spectra, two-thirds of the grains are SiC and the rest of the grains are mainly composed of corundum, hibonite, spinel, and enstatite. Figure 4 clearly shows that most type X grains are characterized by the presence of a significant magnesium peak in their EDX spectra, consistent with having condensed with very high ^{26}Al contents. However, a few mainstream grains also show significant amounts of magnesium, which cannot be distinguished from the X grains as shown in Fig. 4. The high magnesium abundances of these mainstream grains are surprising, given that the aluminum abundances of all measured grains are only up to 4 wt% and that the initial ^{26}Al/^{27}Al ratios of all previously measured mainstream grains are below 0.001 (Zinner 2014). In other words, the concentration of radiogenic magnesium from ^{26}Al decay is expected to be less than 0.004 wt% in mainstream SiC grains, too low to explain the measured amounts of magnesium as being due to ^{26}Al decay to ^{26}Mg (Fig. 4). We, however, cannot exclude the possibility that the high magnesium abundances observed in a few mainstream SiC grains are indigenous magnesium. The isotopic and elemental compositions of the envelopes of the AGB parent stars of mainstream SiC grains are modified by dredge-up of material processed by H- and He-burning in inner shells during thermal pulses (TPs). The ^{25}Mg/^{24}Mg ratio of an AGB stellar envelope increases due to mixing of material processed by the nuclear reaction ^{22}Ne(α,n)^{25}Mg while the star evolves toward advanced TPs. Barium isotopic compositions of mainstream SiC grains (Liu et al. 2014a) constrained the rate with a factor of four uncertainties, and by adopting the lowest allowed rate, model calculations predict only a ~100‰ increase in the δ^{25}Mg/^{24}Mg value of the AGB stellar envelope by the end of the last TP, which is comparable to the analytical uncertainties of the SIMS analyses by Huss et al. (1997), in which no δ^{25}Mg/^{24}Mg isotope anomalies were found.

Although we cannot exclude the possibility of high indigenous magnesium abundances in few mainstream SiC grains, we favor an alternative explanation. Figure 5b clearly shows that the mainstream SiC grains with magnesium abundances greater than 0.19 wt% all have relatively high oxygen abundances. Spinel ($MgAl_2O_4$) and enstatite ($MgSiO_3$) are the most common Mg-rich minerals on the mounts according to the auto-particle EDX results. According to high-resolution SEM-EDX images, the elevated magnesium abundances in some of these mainstream grains were indeed caused by contamination from adjacent Mg-rich silicates and oxides. For the other Mg-rich mainstream grains, no adjacent oxide or silicate grain was found. Thus, their high magnesium concentrations were probably caused by surface magnesium contamination, as we sometimes see heavily Mg-contaminated presolar SiC grains, whose magnesium signals continuously decrease relative to their silicon signals during NanoSIMS analysis of Al-Mg isotopes. Because of the possibility of magnesium contamination that arises from

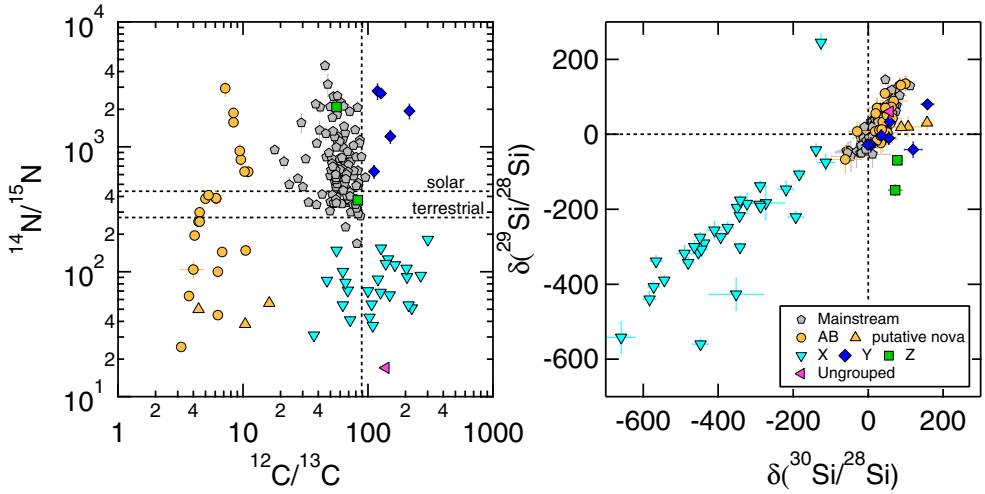

Fig. 3. Carbon, nitrogen, and silicon isotopic compositions of 194 presolar SiC grains that had either magnesium contents higher than 2σ errors and/or that were selected for the micro-Raman study. The dashed lines represent terrestrial isotopic compositions. For $^{14}N/^{15}N$, the solar value (441 ± 5) reported by Marty et al. (2011) is also shown for reference. (Color figure can be viewed at wileyonlinelibrary.com.)

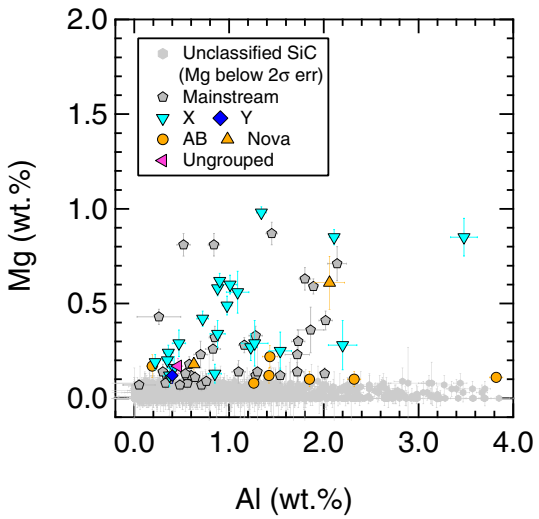

Fig. 4. Magnesium abundances of ~2000 presolar SiC grains plotted against aluminum abundances with 1σ uncertainties. Grains with measurable magnesium (>2σ errors) were analyzed by NanoSIMS and are therefore shown as classified. (Color figure can be viewed at wileyonlinelibrary.com.)

adjacent Mg-rich minerals, in order to confidently identify X grains using the automated SEM-EDX method, presolar grain sample mounts need to be prepared with low grain densities to reduce the degree of grain clustering.

Coordinated Raman and NanoSIMS Data

Raman spectra were obtained with high signal-to-noise ratios on 149 of the 156 single and well-isolated presolar SiC grains; the other 7 mainstream grains showed no Raman peaks. In Fig. 6, the dashed lines represent reference values for the dominant TO peak positions of large well-ordered single crystals of the 3C-, 6H-, and 15R-SiC polytypes (Feldman et al. 1968; Nakashima and Harima 1997). However for 3C, the TO peak is triply degenerate, and for the noncubic polytypes, the degeneracy is lifted by the crystal anisotropy, leading to additional TO peaks. Note that all the reference values are shifted upward by 3 cm^{-1} because of the calibration problem discussed in an earlier section (Raman Spectrometer Calibration).

Figure 6 shows that with the exception of a number of X and a few mainstream grains, most presolar SiC grains show a single Raman peak between 800 cm^{-1} and 792 cm^{-1}. As the dominant TO peaks of non-3C SiC crystals are shifted to much lower wavenumbers, the Raman TO features of these presolar SiC grains are more consistent with the Raman TO frequencies for the 3C polytype but with varying degrees of crystal disorder and defect densities. A few grains lie quite close to the reference value for hexagonal 6H-SiC, which could indicate either the 3C-SiC polytypes with abundant stacking faults or other lattice defects, or well-ordered 6H-SiC grains. Both possibilities can explain one mainstream, one Y, and five X grains in this region. For the AB grains and PNGs in this region, a more likely explanation is an isotope shift in the peak position due to the ^{13}C-enrichment, as will be discussed later (see the ^{13}C-enriched SiC Grain Identification Criteria section).

In contrast to the majority of the 3C-SiC grains, nine mainstream and eight X SiC grains show either

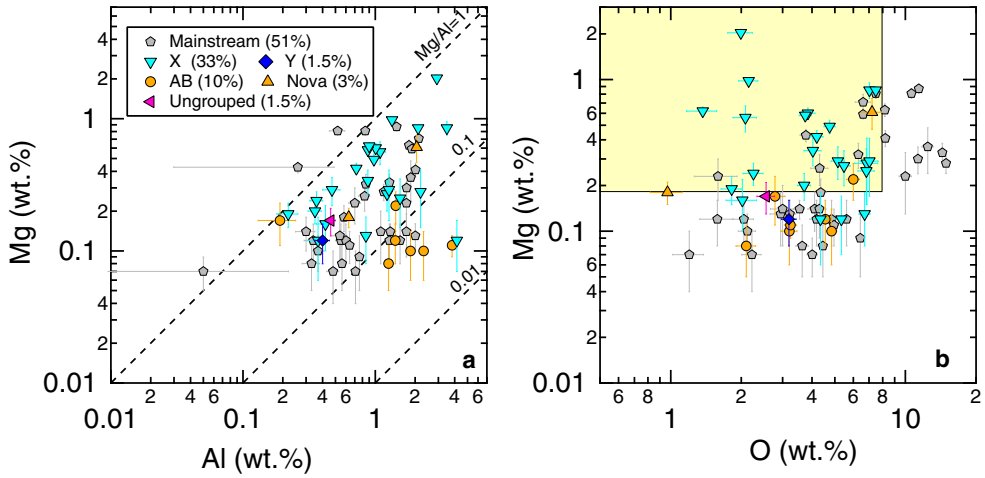

Fig. 5. a) Magnesium abundances plotted against aluminum abundances of presolar SiC grains with measurable magnesium (>2σ errors). b) Magnesium abundances of the same set of grains in (a) plotted against oxygen abundances. The grain data are plotted with 1σ uncertainties. The yellow-shaded area highlights X grain candidates selected by the criteria of >0.19 wt% magnesium and <8 wt% oxygen. (Color figure can be viewed at wileyonlinelibrary.com.)

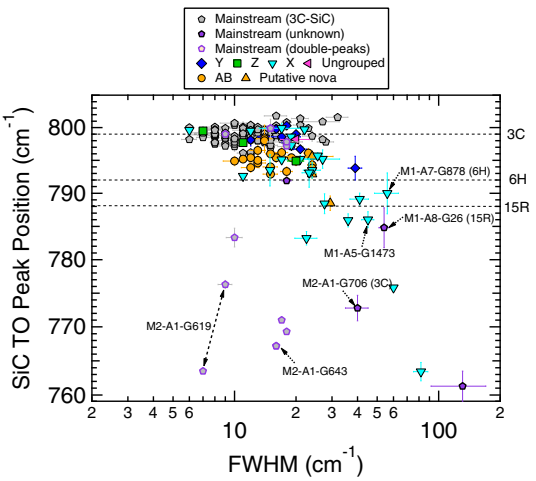

Fig. 6. Raman TO peak positions of 156 presolar SiC grains with measurable Raman signals plotted against FWHM values with 1σ uncertainties. The dashed lines represent theoretical predictions (shifted upward by 3 cm^{-1}) for the TO peak positions of different SiC polytypes. Grains lying close to the 6H-SiC theoretical line could be either 6H-SiC or highly disordered 3C-SiC. Six of the presolar SiC grains that show much lower shifted TO peaks are labeled. The double peaks of the mainstream grain, M2-A1-G619, are highlighted in the figure.

much lower shifted and broadened Raman peaks, or double TO peaks (Fig. 6). Several representative Raman spectra are shown in Fig. 7. Five out of these nine mainstream grains had comparatively narrow but double peaks, which could indicate 4H- and 3C-SiC, 6H- and 3C-SiC, and 2H- and 4H-SiC intergrowths, in addition to the 2H- and 3C-SiC intergrowth found in the previous TEM study of Daulton et al. (2003). However, although the dominant TO peaks of hexagonal polytypes, including 2H-, 4H-, and 6H-SiC, are at lower wavenumbers by varying amounts, all these hexagonal polytypes also have another TO peak near 796 cm^{-1}. The relative intensity of the TO peaks varies with the crystal orientation relative to the illumination. Thus, the double peaks observed in these Raman spectra could alternatively indicate hexagonal polytypes. Note that a higher concentration of stacking faults and crystal disorder can be excluded in explaining the Raman features of these five mainstream SiC grains because, as will be shown later, while stacking faults and crystal disorder can significantly downward shift the Raman peaks of SiC grains, concomitant peak broadening is also expected. In contrast, the TO peak widths of these five grains are well within the range of 3C-SiC mainstream grains in the upper region. Based on the previous TEM study of Daulton et al. (2003), the most likely structures for these are 3C and 2H intergrowths, but this attribution remains to be confirmed with future TEM studies.

Three mainstream and wavenumbers eight X grains have Raman peaks that are significantly broadened (FWHM >20 cm^{-1}), and shifted to much lower wavenumbers than the 3C-SiC position. The broadened peaks of these grains could be explained by enhanced trace element abundances and/or the merger of multiple TO peaks in the Raman spectra of non-3C SiC grains, as likely in the case of M1-A7-G878 that is confirmed to be a well-ordered 6H-SiC by TEM analysis (see Discussion section). On the other hand, grain M2-A1-G706 has a uniquely well-structured pattern (Fig. 7) composed of a series of intense peaks below 700 cm^{-1}

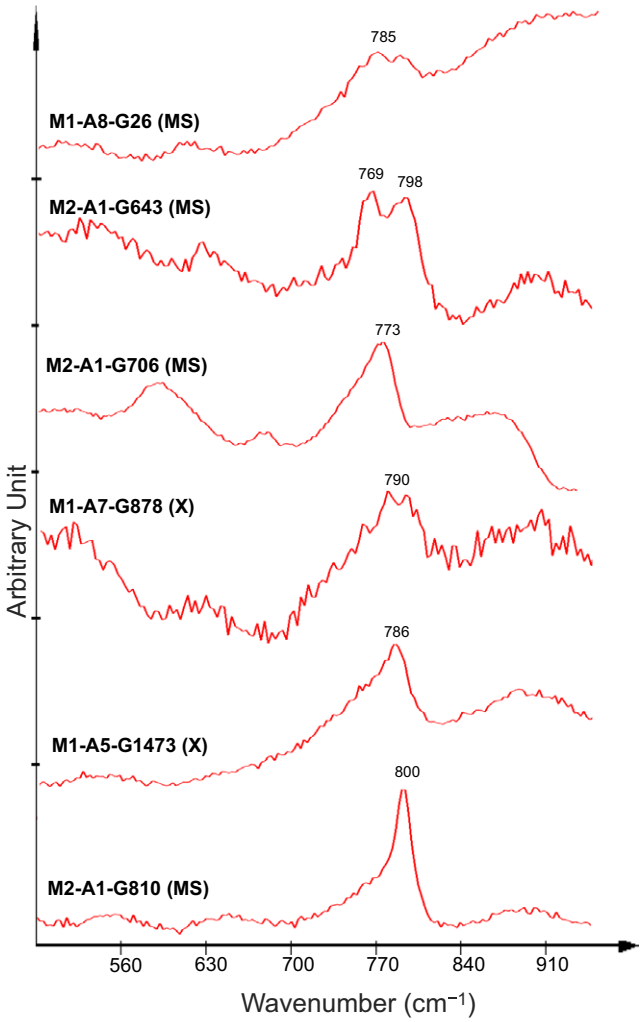

Fig. 7. Raman spectra of selected presolar SiC grains. The mainstream (MS) grain, M2-A1-G810, with a sharp TO peak at 800 cm^{-1} that is typical of 3C-SiC polytype is shown at the bottom for reference. (Color figure can be viewed at wileyonlinelibrary.com.)

and one additional asymmetric peak at ~900 cm^{-1}. These peaks can be attributed to longitudinal acoustic and longitudinal optical modes, respectively (Nakashima and Harima 1997). The breadth and intensity of these peaks suggest that a significant amount of twinning or stacking disorder is likely present in this grain.

TEM Data

The extracted FIB section of type X grain, M1-A7-G878, shows two main lobes that are narrowly connected at the top (Fig. 8). Both lobes contain multiple subgrains, the largest of which is a 30 nm Fe-, Ni-, Si-, N-rich grain. Others include Ti-rich and (Al,Mg)N phases. Although some N-rich subgrains are present, the EDX mapping indicates that the majority of the incorporated aluminum, magnesium, and nitrogen atoms are spatially correlated, and distributed throughout the SiC lattice in solid solution. Multiple SAEDPs were obtained from the left lobe. The three patterns shown in Fig. 8 index to the [8 10 1], [9 18 $\bar{1}$], and [8 22 $\bar{1}$] zones of the 6H polytype, respectively. A summary of the diffraction analysis and rationale for rejecting 3C is provided in the supporting information. Patterns 8d and 8f could be alternately indexed to 3C zones, but pattern 8e would require an excessively large deviation in the d-spacing ratios (1.07 compared 1.0) and angles (63° compared to 60°) to the fit to 3C. A single diffraction pattern obtained from the left lobe was also consistent with the 6H polytype, but at a different orientation (distinct crystallite) than the right lobe. Thus, both the TEM results and the Raman data (Fig. 6) are in good agreement that grain M1-A7-G878 is 6H. In addition, its broadened TO peak is highly likely to be caused by the presence of high abundances of nitrogen, magnesium (probably radiogenic ^{26}Mg), and aluminum impurities (Fig. 8c) in the SiC lattice (see the Raman Peak Broadening in Presolar SiC Grains section for details) and/or the merger of multiple TO peaks of the 6H-SiC polytype.

Grain M1-A8-G26, an isotopically typical mainstream SiC, has a quite rare and distinctive needle shape (0.4 × 4 μm, Fig. 9f), similar to the 2H needle-shaped grain reported by Daulton et al. (2002). The TEM analysis of the cross section of grain M1-A8-G26 (Fig. 9) shows that the grain shape is very irregular, even on the bottom surface pressed into the gold substrate that was not exposed to the SIMS ion beam. The interior of the grain contains both subgrains and a void. The electron diffraction patterns have sharp spots indicative of good crystalline order. The lowest order polytype that provides a consistent indexing for all three zones shown is 15R, consistent with its Raman TO peak position as shown in Fig. 6. The 3C polytype in particular can be excluded for the zones as shown in Figs. 9c and 9d, because the measured d-spacings would require an unexplained change in the calibration constant of the camera by 5% for the 9d pattern only, despite care in acquisition to keep the microscope conditions constant; and the measured angle of 63.5° between planes in the 9e pattern is too far from the 54.7° expected for the best-fit pattern for 3C. In addition, the angles between the zones are inconsistent with respect to the 3C structure. (See the supporting information for additional details). The grain composition determined from EDX shows minor titanium, aluminum, and nitrogen, but no detectable magnesium. The elongated subgrain visible in Fig. 9a

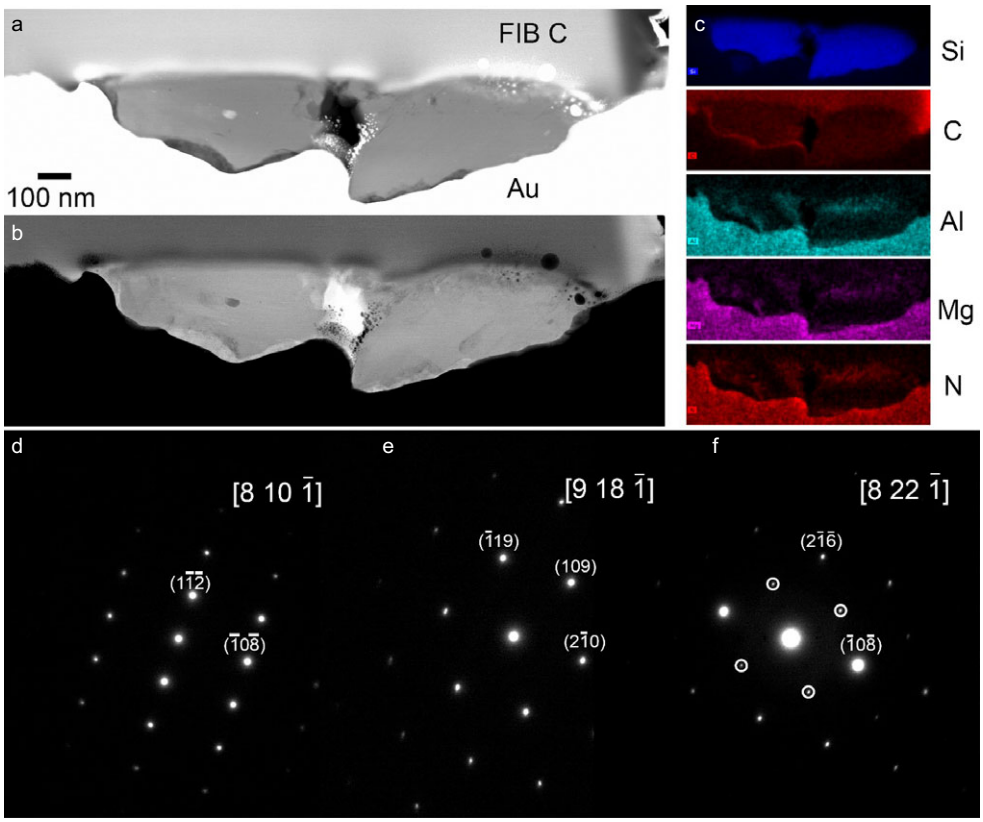

Fig. 8. TEM analysis of grain M1-A7-G878. a) HAADF STEM. b) BF STEM. c) STEM-EDX elemental maps. d–f) SAEDPs from zones [8 10 −1], [9 18 −1], and [8 22 −1] of the 6H structure, respectively. Double diffraction spots at ½(1 −2 −14) positions in (f) are outlined with white circles. The grain section shows two lobes, narrowly connected at the top of the grain. A 30 nm Fe, Ni, Si, N-rich subgrain in the left lobe appears as a bright spot in (a) and dark spot in (b). Additional smaller subgrains are present though only discerned in higher resolution images, including at least one (Al,Mg)N and a Ti-rich grain. Most of the aluminum, magnesium, and nitrogen impurities appear to be colocated in solid solution in the SiC lattice, rather than as distinct subgrains (c). Note that the apparent presence of aluminum, magnesium, and nitrogen in the gold substrate is an artifact of the increased background bremsstrahlung counts from the higher Z material. (Color figure can be viewed at wileyonlinelibrary.com.)

(white arrow) contains titanium, aluminum, nitrogen, and silicon.

Grain M2-A1-G706 is another isotopically typical mainstream grain with a complex Raman spectrum (Fig. 7). The TEM observations of grain M2-A1-G706 reveal a well-crystallized grain with some twinning or double diffraction (Fig. 10). A linear crack in the grain is visible (Fig. 10a) cutting across most of the grain, although the crystal orientation appears to be maintained across the crack, as the diffraction patterns were consistent on both sides of the crack. The primary diffraction spot spacings and angle between the zones are consistent with the 3C polytype (see the supporting information for more detail). The extra spots, indicative of twinning or other superstructures, are likely related to the complex Raman spectrum. The degree of stacking disorder or twinning seen in the TEM is somewhat less than expected for the degree of deviation of the Raman spectrum obtained from a single 3C-SiC crystal, but it should be noted that the Raman observations were made in a geometry orthogonal to that of the extracted FIB slice. The TEM data were constrained to measuring defects and stacking disorder in a narrow tilt range (±25°) around the axis of the FIB section, so not every possible direction of stacking disorder could be observed. EDX elemental mapping and spectra show SiC with minor aluminum and nitrogen abundances, and no detectable magnesium.

DISCUSSION

CCSN SiC Grain Identification Criteria

CCSN SiC Grain Identification by BSE-EDX Analysis

By setting a threshold for the oxygen abundance at <8 wt%, most of the Mg-contaminated mainstream grains can be filtered out from the X grain candidate pool (Fig. 5b). Obviously, the reliability of identifying X

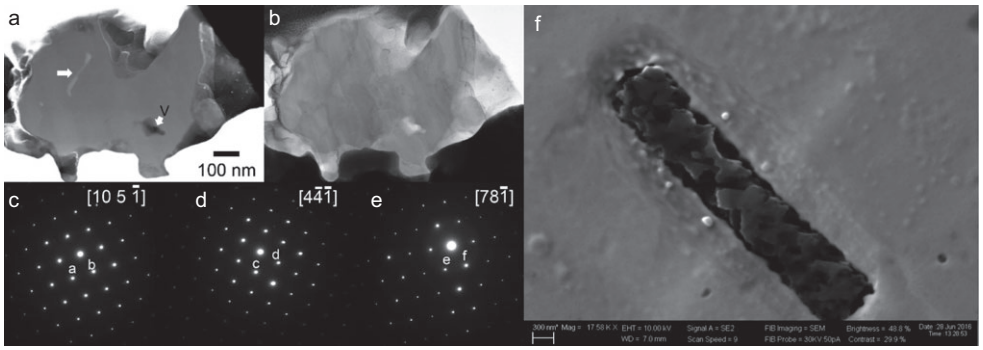

Fig. 9. TEM analysis of grain M1-A8-G26. a) HAADF STEM image. The white arrow labeled with a V indicates the location of a void in the grain interior. The unlabeled white arrow indicates the location of a subgrain that is rich in titanium, aluminum, and nitrogen. b) BF STEM image. c–e) SAEDPs that index to the 15R polytype, with labels that refer to planes: a (0 1 5); b (−1 1 – 5); c (104); d (0 1 – 4); e (107); f (018). f) SEM image (The lowered gold substrate in the upper part of the image is due to Cs^+ sputtering during NanoSIMS analysis, as only half of the grain was used for the analysis).

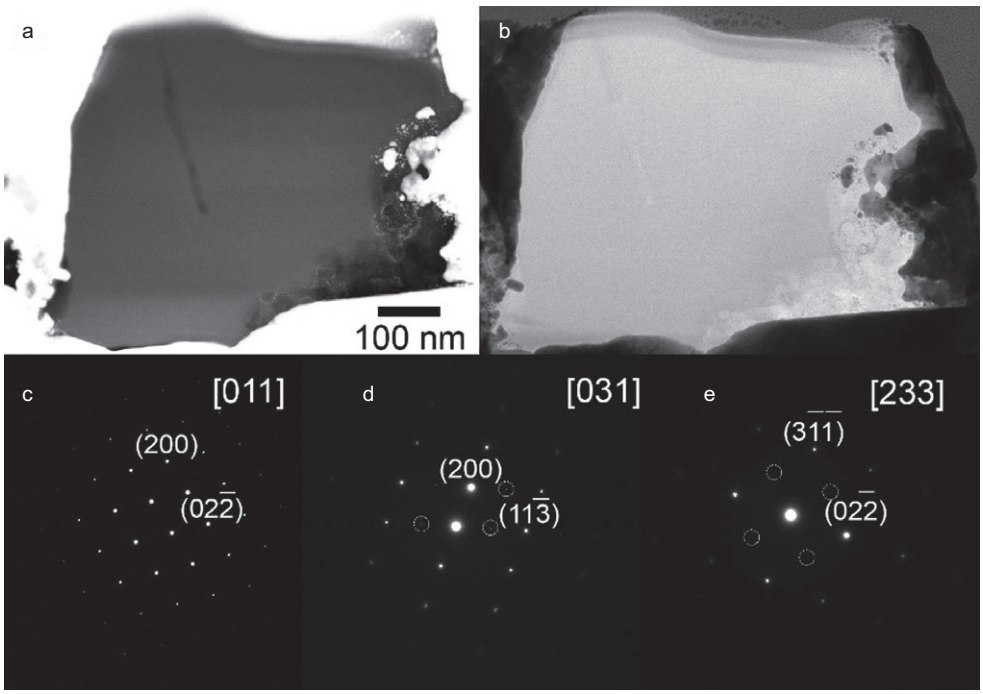

Fig. 10. TEM analysis of grain M2-A1-G706. a) STEM HAADF image. b) BF STEM image. The diagonal line through the grain from upper left to the middle is a crack. c–e) SAEDPs are indexed to 3C zones, with double diffraction or twin spots outlined with circles.

grains by the BSE-EDX analysis depends strongly on the threshold chosen for the magnesium abundance. To maximize both detection efficiency and reliability, we have set the threshold at >0.19 wt%. Based on these criteria (the yellow-shaded area in Fig. 5b), we are left with 19 X, 1 nova, 1 AB, and 7 mainstream grains, corresponding to ~70% X SiC grains, a factor of 35−70 higher than their natural 1−2% abundance among presolar SiC grains. In fact, the four X grains with lower magnesium contents are all found to be clumped together with more than one adjacent mainstream SiC grain in their NanoSIMS ion images. Their relatively low-magnesium abundances are therefore most likely to have been caused by dilution from surrounding mainstream SiC grains that are typically Mg-poor, but Al-rich (Fig. 5a).

To summarize, our study of ~2000 presolar SiC grains demonstrates that the automated BSE-EDX analysis is a robust method for identifying presolar X, C1, C2, and PNG grains with initial $^{26}Al/^{27}Al$ ratios

higher than 0.01. Under our chosen analytical conditions, the detection accuracy is primarily affected by magnesium contamination, and the detection efficiency is solely affected by signal dilution from adjacent Mg-poor SiC grains. Based on the criteria of >0.19 wt% magnesium and <8 wt% oxygen abundances, we were able to identify 1 PNG (~0.05%) and 19 X (~1%) grains out of ~2000 SiC grains with ~70% detection accuracy (1 PNG and 19 X grains out of 28 candidates) and ~80% detection efficiency (4 unidentified X grains out of 23 X grains). Moreover, the detection accuracy and efficiency can be further improved, if spinel and enstatite in the SiC acid residue can be more effectively removed and if grains are better dispersed and separated on the gold substrate.

CCSN SiC Grain Identification by Micro-Raman Analysis

Presolar X grains and PNGs generally have Raman peaks that are broadened and shifted to lower wavenumbers relative to mainstream grains (Fig. 6). Previous TEM studies of X grains found that while mainstream grains are usually single crystals, X grains are commonly composed of small crystallites on the order of 10–100 nm with the presence of twinning (Stroud et al. 2004; Hynes et al. 2010), which could result in lower shifted and broadened Raman peaks. On the other hand, the inclusion of small domains of noncubic polytypes is one possible explanation for the lower shifted peak positions. If the TO peaks of two different SiC polytypes or the multiple TO peaks of non-3C SiC polytypes are broadened and/or close in position, they are expected to merge to a broadened peak that appears in between the two TO peaks, i.e., shifted to wavenumbers lower than the 3C-SiC TO peak (grains M1-A5-1473 and M1-A7-G878 in Fig. 7). For instance, Stroud et al. (2015) showed variations in stacking disorder and polytype at sub-μm spatial scale in the very large "Bonanza" X grain (grain LU-13) with a TO peak centered at 789 cm^{-1} (Wopenka et al. 2010). In addition, Hynes et al. (2010) observed a close intergrowth between 3C- and 2H-SiC that switches back and forth between the two through one X grain, which could result in lower shifted and broadened Raman features. However, Daulton et al. (2003) showed 2H-SiC and 3C-SiC intergrowths were common in mainstream grains (~17% of the 500 SiC grains studied), and not specific to X grains (1% of the analyzed grains). Thus, if the polytype intergrowth indeed shifts the Raman peak of presolar SiC grains to lower wavenumbers, it is not limited to X grains. To summarize, the Raman features of X grains could result from enhanced trace element abundances, higher densities of stacking defects/faults, and/or higher abundances of polytype intergrowth and non-3C SiC polytypes with merged multiple TO peaks at different wavenumbers.

Thus, criteria, including elemental composition and Raman peak width, should be combined with Raman peak shift for identifying X grains. As shown in Fig. 6, the Raman TO peak width of presolar SiC can be used as an additional indicator for further separating Mg-rich mainstream SiC grains from the X grain candidate pool. In Fig. 6, 14 out of 22 X grains and all the three PNGs show FWHM values higher than 20 cm^{-1}, while <10% of the mainstream grains show such broadened peaks. We collected Raman spectra from two of the seven mainstream grains, as shown in the yellow-shaded area of Fig. 5b (grains M2-A1-G49 and M2-A1-G322 in Tables S1 and S2), that cannot be filtered out from the X grain candidate pool based on the BSE-EDX analysis. In fact, both grains had a TO peak at 799 cm^{-1} with a FWHM value of 14 cm^{-1}, which corresponds to ~90% possibility of being mainstream grains (Fig. 6). Thus, the detection accuracy of X grains can be significantly improved to above 70% by correlated BSE-EDX and Raman analyses. To conclude, the majority of X grains (~80%) can be identified by the correlated BSE-EDX and micro-Raman analyses with >70% confidence.

^{13}C-Enriched SiC Grain Identification Criteria

The frequencies of vibrational modes of a solid are a function of the interatomic force constants and the atomic masses. Consequently, significant changes in the average atomic mass due to isotopic substitution will lead to changes in the frequencies of the vibrational modes that can be measured by Raman spectroscopy. Such isotope effects have been previously investigated in diamond, germanium, and α-Sn by Raman spectrometry (Fuchs et al. 1991; Hass et al. 1992; Wang et al. 1997); these studies demonstrated that virtual crystal approximation (VCA) can be used to roughly describe the effect caused by the presence of different isotopes in sublattices of a solid. In a SiC virtual crystal, each SiC lattice site is assumed to be occupied by identical carbon atoms with an average mass of $\overline{M}_c = 12 + x/100$ amu, where x is the percentage of ^{13}C, and an average mass of $\overline{M}_{Si} = 28 + y_1/100 + 2y_2/100$ amu for silicon atoms, where y_1 is the percentage of ^{29}Si and y_2 is the percentage of ^{30}Si. For such a virtual crystal, the TO mode frequency is proportional to the inverse of the square root of the reduced mass, M_μ (Rohmfeld et al. 2001), which can be written as

$$\omega_{TO} \propto M_{\mu}^{-1/2} \quad (2)$$

where $M_{\mu} = \overline{M}_c \times \overline{M}_{Si}/(\overline{M}_c + \overline{M}_{Si})$.

Figure 6 clearly shows that the TO peak positions of ^{13}C-enriched AB grains and PNGs are shifted to lower wavenumbers relative to those of less ^{13}C-rich mainstream SiC grains. By plotting TO peak position versus ^{12}C/^{13}C, Fig. 11 better illustrates that the shift in the TO peak position depends strongly on the carbon isotopic ratio. Because 3C-SiC with normal carbon and silicon isotopic composition has a reduced mass of 0.34485 with the TO phonon frequency at 796.2 cm^{-1}, the scaling factor of Equation 2 can be directly calculated for 3C-SiC to be 2308.86. To better illustrate the effect of isotope substitution, the overall VCA predictions are increased by 3 cm^{-1} to account for the calibration problem discussed in the Raman Spectrometer Calibration section. In Fig. 11, the median data point (green circle) for the ^{13}C-enriched grains falls right on the VCA curve. Thus, the average peak shift seen in ^{13}C-enriched SiC grains is well explained by the change in the atomic mass of SiC due to isotope substitution. As SiC grains with ^{12}C/^{13}C $\leq$ 10 show Raman peaks at lower wavenumbers than most of the mainstream SiC grains (80 out of the 83 mainstream grains) due to their increased atomic mass, micro-Raman analysis can therefore be used as a novel technique to nondestructively identify highly ^{13}C-enriched presolar SiC grains. Finally, we want to emphasize that although the Raman parameters for the ^{13}C-enriched AB grains are overlapped with those of 50% of the X grains (Fig. 6), such an overlap only slightly lowers the detection reliability by ~10%, as the natural abundance of X grains is a factor of four to five lower than that of AB grains (Zinner 2014). In addition, Fig. 5b shows that X grains can be well separated from the majority of AB grains by their higher magnesium concentrations. Thus, AB grains can be identified as Mg-poor SiC grains with the TO peak lower than ~797 cm^{-1} with ~80–90% confidence.

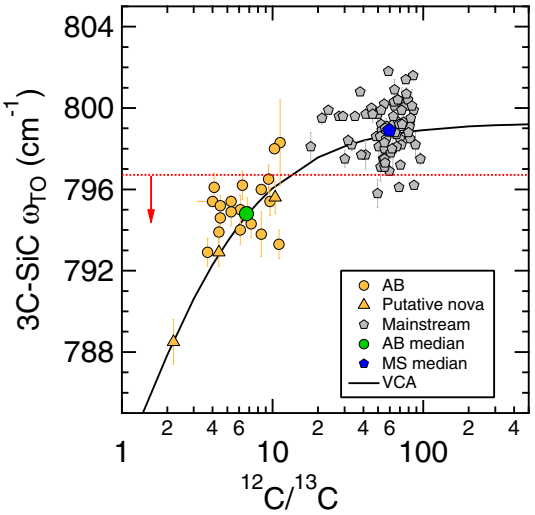

Fig. 11. Raman TO peak positions of 83 mainstream grains with the 3C structure indicated by their TO Raman peak positions, 20 AB grains, and 3 PNGs are plotted against carbon isotopic ratios. All data are plotted with 1σ uncertainties. The red dashed line and arrow represent the criterion for selecting PNG and AB grains. (Color figure can be viewed at wileyonlinelibrary.com.)

Raman Peak Broadening in Presolar SiC Grains

In addition to the effect of isotope substitution, previous studies on the effects of crystal stacking faults (Rohmfeld et al. 1998), temperature (Olego and Cardona 1982; Bauer et al. 2009), and ion implantation-induced crystal damage (Nakashima et al. 2005) on SiC phonon frequencies, all showed a shift in the Raman peak frequencies to lower values and/or peak broadening. On the other hand, minor element impurities could shift the Raman peak of SiC to higher values, but the corresponding effects are not quantified because the impurity concentrations in SiC were not determined in most of the published studies. For instance, Lin et al. (2012) showed that the TO peak of N-doped 6H-SiC shifts to higher wavenumbers by more than 2 cm^{-1} compared to that of the undoped sample in their study, while Li et al. (2010) found that by increasing the nitrogen gas pressure by more than three orders of magnitude during doping, the corresponding TO peak shifts to higher values only by 0.6 cm^{-1}. In comparison, as will be discussed later, our correlated NanoSIMS and Raman studies of presolar SiC grains show that the nitrogen impurity, at ~1 wt% levels in presolar SiC, only significantly broadens the TO peak of 3C-SiC without affecting the peak position.

Although isotope substitution is the dominant cause of downward shifts in the TO peak for AB grains and PNGs, its effect should be negligible on the TO peak positions of mainstream, Y, Z, and X SiC grains because these groups of grains generally show much smaller or no enrichments in ^{13}C and the variations in silicon isotopes are also too small to cause any observable effects. This is because the reduced masses for these groups of grains are essentially the same as those of SiC with pure ^{12}C and normal silicon isotopic compositions (M_{μ} = 8.409). In fact, the median value of the TO peak positions of our measured mainstream SiC grains is ~3 cm^{-1} higher than the theoretical value of 796.2 cm^{-1} for 3C-SiC, which is consistent with the offset indicated by terrestrial 6H-SiC and hexagonal BN data (see the Raman Spectrometer Calibration section).

In addition, a few mainstream 3C-SiC grains also show downward shifted TO peaks relative to the theoretical predication by up to 4 cm^{-1} (Figs. 6 and 8). As mentioned previously, a number of factors other than isotopic substitution could have downward shifted the Raman peaks of the mainstream SiC grains by a few wavenumbers, such as crystal stacking faults and ion implantation.

The isotope variation can cause phonon peaks to downward shift in wavenumber and also to broaden without changing the crystal structure, i.e., SiC polytype (Hass et al. 1992; Spitzer et al. 1993; Rohmfeld et al. 2001). Experimental and theoretical studies showed that for 6H-SiC with $^{12}C/^{13}C = 1$, the first-order TO peak can be broadened by ~7 cm^{-1} and that the isotope-induced peak broadening is almost a linear function of ^{13}C abundance in the range of carbon isotopic ratios investigated in our study (Rohmfeld et al. 2001). This peak broadening effect of isotope substitution on the SiC TO peak reported in Rohmfeld et al. (2001), however, shows that isotope substitution can only cause ~3 cm^{-1} peak broadening for a median carbon isotope ratio of 6, corresponding to a 4 cm^{-1} downward shift in the TO peak (Fig. 11). Thus, although the effect of isotope-induced broadening explains the significantly higher median FWHM (15.5 cm^{-1}) of the 20 3C-SiC AB grains and three 3C-SiC PNG relative to that (11.0 cm^{-1}) of the 83 mainstream 3C-SiC grains, isotope substitution alone is insufficient in explaining the range of peak broadening observed for both mainstream and AB grains (black solid line in Fig. 12a).

In addition to isotope substitution, another well-studied factor that can cause both Raman peak shift and broadening is stacking faults. As shown by Daulton et al. (2003), stacking faults are quite common in presolar SiC grains and more than 35% of the 3C-SiC grains in their study had visible stacking faults. Rohmfeld et al. (1998) found that the linewidth of polycrystalline 3C-SiC with stacking faults is naturally more broadened due to variation in the local atomic configuration compared to a single 3C-SiC crystal. Their experimental data are shown as a red dotted line in Fig. 12a for reference. While stacking faults can generally cause slightly greater peak broadening than isotope substitution with respect to the same peak position, this effect does not completely explain the much larger degree of peak broadening observed in the majority of the grains.

Elemental impurities seem to be the most likely factor in causing peak broadening for the mainstream SiC grains without significant peak shifts, as shown in Fig. 12b. The nitrogen abundance was calculated based on the NanoSIMS ion imaging data by adopting a relative sensitivity factor of nitrogen to silicon of 10 reported by Huss et al. (1997), in which a diamond standard with ~200 ppm nitrogen was used. For the mainstream 3C-SiC grains, in Fig. 12b, the correlation coefficient (R) between the TO peak width and the nitrogen abundance is 0.77, a strong indication that the peak broadening is dominantly caused by the incorporation of nitrogen into the grains. Interestingly, Fig. 12b shows that grains with peak widths greater than 20 cm^{-1} either have nitrogen concentrations higher than 3 wt% or are highly enriched in ^{13}C ($^{12}C/^{13}C < 5$, i.e., >7 wt% ^{13}C). In addition, the latter show much more significant peak shifts (>5 cm^{-1}) than the former (<3 cm^{-1}). These correlations, along with the TEM data discussed previously, strongly indicate that nitrogen impurity mainly exists in the SiC lattice in solid solution, which likely caused the Raman peak broadening without substantial peak shifts. Furthermore, as aluminum is quite abundant in presolar SiC (Fig. 4) and roughly correlated with nitrogen in presolar SiC (fig. 12 of Huss et al. 1997), the fact that nitrogen plays a dominant role in determining the peak broadening strongly indicates that aluminum coexists with nitrogen in the solid solution, which is strongly supported by the spatially correlated nitrogen and aluminum EDX maps of grain M1-A7-G878 (Fig. 8). Thus, impurities other than nitrogen, highly likely including aluminum, probably also contribute to the broadening of the TO peaks of presolar SiC grains.

Formation of SiC Grains in Stars

A previous TEM study of ~500 SiC grains reported a polytype distribution of 80% 3C-SiC, 17% 2H- and 3C-SiC intergrowth, 3% 2H-SiC, and <1% one-dimensionally stacking disordered SiC (Daulton et al. 2003). As the grains in the Daulton et al. study were not classified isotopically and mainstream grains are the dominant presolar SiC type, the TEM results can be compared to the Raman data for the 99 mainstream SiC grains in our study, which shows a distribution of ~90% 3C-SiC (84 MS 3C-SiC and 2 MS SiC with unknown polytypes out of 93 MS SiC, Table S2). Generally speaking, our Raman data agree with the previously published TEM data on the fact that 3C-SiC is the dominant polytype for mainstream SiC grains. In an earlier study of large presolar SiC grains by Virag et al. (1992), more than 25% of the grains did not show any Raman features. Only 7% of presolar SiC grains have featureless Raman spectra in our study, possibly reflecting the higher detection efficiency of the Raman spectrometer used in our study, or an intrinsic difference to the larger grains in the Virag et al. (1992) studies, e.g., greater crystal disorder, thicker amorphous rims around, and/or amorphous carbon contamination on the grain surfaces.

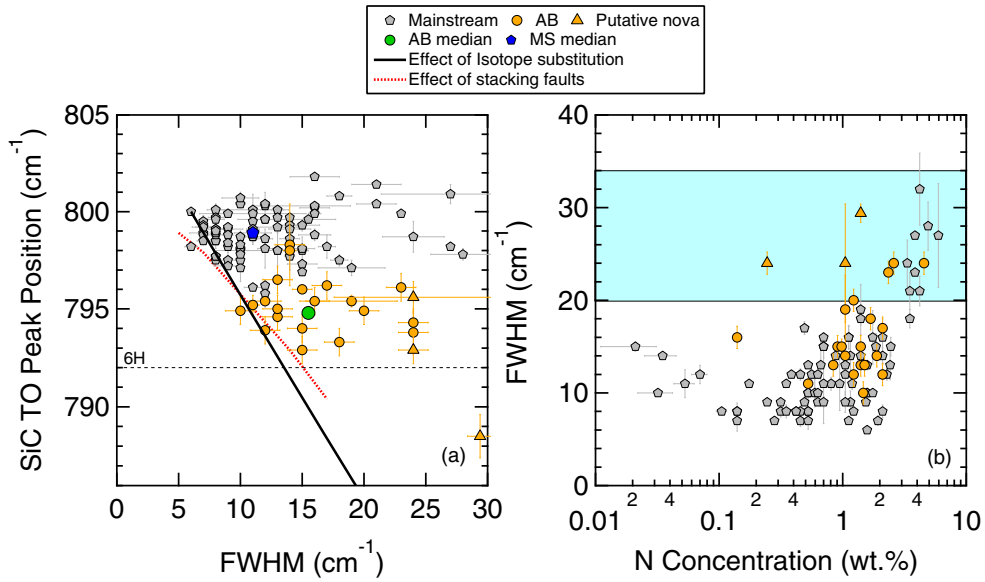

Fig. 12. a) Raman TO peak positions of mainstream and ^{13}C-enriched 3C-SiC are plotted against their corresponding linewidths (FWHM). b) The linewidths (FWHM) are plotted against their corresponding nitrogen concentrations for the same set of grains as in (a). The nitrogen concentration is calculated by adopting the relative sensitivity factor of nitrogen to silicon of 10 reported by Huss et al. (1997). (Color figure can be viewed at wileyonlinelibrary.com.)

Finally, it should be pointed out that the Raman features of mainstream, AB, Y, and Z grains are quite similar if the AB data are corrected for the effect of isotope substitution. In contrast, most of X grains from CCSNe show much more downward shifted and broadened TO peaks, indicating either increased disorder in the form of impurities and stacking defects/twins, or higher order non-3C polytypes, as confirmed by our coordinated TEM analysis. Based on these facts, we conclude that the condensation environments were remarkably similar in the parent stars of most presolar SiC grains, the main exceptions being environments in the parent supernovae of X grains. The X grains condensed under a greater range of conditions, including higher temperature and/or higher pressure conditions that resulted in higher concentrations of subgrains/impurity solid solutions and stacking defects, and an enhanced percentage of higher order non-3C SiC polytypes.

CONCLUSIONS

We have developed a novel, rapid, and nondestructive analytical method for identifying rare subgroup SiC grains using a combination of BSE-EDX analysis and Raman spectroscopy. This nondestructive method can preserve identified rare subgroup SiC grains for further analysis with other instruments, such as NanoSIMS, TEM, and resonance ionization mass spectrometry (e.g., Liu et al. 2017b). Based on our coordinated BSE-EDX, NanoSIMS, micro-Raman studies of a large number of presolar SiC grains, we come to the following conclusions.

1. The quantitative magnesium abundance and the TO peak position and width of presolar SiC grains determined by standardized EDX and Raman analyses can be used to reliably locate supernova grains. We mapped out 3 × 3 mm areas on two gold mounts on which a Murchison SiC residue had been dispersed and pressed, and identified ~2000 SiC grains with the automated particle analysis (in the optional AZtecFeature module) in the AZtec BSE-EDX system in the SEM in two weeks. Subsequent NanoSIMS analysis of 70 of those SiC grains with magnesium abundances that were greater than 2σ errors (~0.06 wt%) identified 2 PNGs and 23 X grains. Based on the criteria of >0.19 wt% magnesium and <8 wt% oxygen, we identified 1 PNG and 19 X grains, and missed one PNG and four X grains due to magnesium signal dilution from nearby mainstream SiC grains. In addition, X grains showed more broadened (> ~20 cm^{-1}) and/or lower shifted Raman peaks than mainstream grains, which can be used to distinguish Mg-rich mainstream grains from Mg-rich X grains. Consequently, correlated BSE-EDX and micro-Raman analyses can be used to identify X grains with ~80% detection efficiency with >70% confidence. The detection accuracy and efficiency can be further improved by more effectively

removing spinel and enstatite minerals from the SiC acid residue and also by reducing the grain density on the mount to avoid grain clumping.

2. Our micro-Raman study of 156 presolar SiC grains showed that 3C-SiC is the dominant polytype, in good agreement with previous TEM studies. Also, coordinated TEM analysis of one X and two mainstream grains with much lower shifted Raman TO peaks confirms the higher order non-3C SiC polytype structures in two of the three grains, 6H and 15R, inferred from their Raman spectra. A third grain, with lower shifted TO Raman, and additional non-TO peaks, has TEM data consistent with the 3C structure with some stacking defects/twinning. Thus, Raman spectroscopy of these grains of micrometer to submicrometer sizes is a good way to search for non-3C polytypes, but because extra peaks in the Raman spectra can appear from either noncubic polytypes or stacking defects in a 3C crystal, TEM should be used for definitive structure determination.
3. Our micro-Raman results further demonstrated that with respect to mainstream SiC grains, the downward shifted Raman phonon frequencies of highly ^{13}C-enriched presolar SiC grains with concomitant peak broadening are dominantly caused by atomic mass-dependence of lattice vibrations. Thus, micro-Raman analysis can be used to robustly identify ^{13}C-enriched presolar SiC grains such as AB, C2, and PNGs with $>90\%$ confidence.
4. The effect of isotope composition on Raman spectra for presolar SiC grains other than AB, C2, and PNGs is negligible. Mainstream SiC grains only showed small frequency shifts (<3 cm^{-1}) that are not correlated with peak broadening. In addition, the peak widths of the mainstream grains studied are significantly correlated ($R = 0.77$) with their nitrogen concentrations, indicating that the peak broadening is mainly caused by higher concentrations of elemental impurities, predominantly nitrogen and possibly aluminum.
5. After correcting for the effect of isotope substitution, mainstream, AB, Y, and Z grains in general show quite similar Raman features, while many of the X grains show distinctive features indicating significantly different condensation environments in their parent supernovae, e.g., much higher temperatures and densities, and perhaps much shorter condensation timescales, relative to parent stars of other types of presolar SiC grains.

Acknowledgments—We thank Drs. J. Armstrong and E. Bullock for technical support on the SEM, and Drs. Phillip Heck and Tyrone Daulton for constructive reviews that helped improve the paper. This work was supported by NASA's Cosmochemistry program (grant NNX10AI63G to LRN).

Editorial Handling—Dr. A. J. Timothy Jull

REFERENCES

Alexander C. M. O'D. 1993. Presolar SiC in chondrites – How variable and how many sources? *Geochimica et Cosmochimica Acta* 57:2869–2888.

Amari S., Nittler L. R., and Zinner E. 2001a. Presolar SiC grains of type A and B: Their isotopic compositions and stellar origins. *The Astrophysical Journal* 559:463–483.

Amari S., Gao X., Nittler L. R., and Zinner E. 2001b. Presolar grains from novae. *The Astrophysical Journal* 551:1065–1072.

Anders E. and Zinner E. 1993. Interstellar grains in primitive meteorites: Diamond, silicon carbide, and graphite. *Meteoritics* 28:490–514.

Bauer M., Gigler A. M., Huber A. J., Hillenbrand R., and Stark R. W. 2009. Temperature-depending Raman line-shift of silicon carbide. *Raman Spectroscopy* 40:1867–1874.

Choi B.-G., Huss G. R., Wasserburg G. J., and Gallino R. 1998. Presolar corundum and spinel in ordinary chondrites: Origins from AGB stars and a supernova. *Science* 282:1284–1289.

Daulton T. L., Bernatowicz T. J., Lewis R. S., Messenger S., Stadermann F. J., and Amari S. 2002. Polytype distribution in circumstellar silicon carbide. *Science* 296:1852–1855.

Daulton T. L., Bernatowicz T. J., Lewis R. S., Messenger S., Stadermann F. J., and Amari S. 2003. Polytype distribution in circumstellar silicon carbide: Microstructural characterization by transmission electron microscopy. *Geochimica et Cosmochimica Acta* 67:4743–4767.

Feldman D. W., Parker J. H., Choyke W. J., and Patrick L. 1968. Phonon dispersion curves by Raman scattering in SiC polytypes 3C, 4H, 6H, 15R, and 21 R. *Physical Review* 173:787–793.

Fryling M., Frank C. J., and McCreery R. L. 1993. Intensity calibration and sensitivity comparisons for CCD/Raman spectrometers. *Applied Spectroscopy* 47:1965–1974.

Fuchs H. D., Grein C. H., Thomsen C., and Cardona M. 1991. Comparison of the phonon spectra of ^{70}Ge and natural Ge crystals: Effects of isotopic disorder. *Physical Review B* 43:4835–4842.

Groopman E., Zinner E., Amari S., Gyngard F., Hoppe P., Jadhav M., Lin Y., Xu Y., Marhas K., and Nittler L. R. 2015. Inferred initial ^{26}Al/^{27}Al ratios in presolar stardust grains from supernovae are higher than previously estimated. *The Astrophysical Journal* 809:31.

Gyngard F., Zinner E., Nittler L. R., Morgand A., Stadermann F. J., and Hynes K. M. 2010. Automated NanoSIMS measurements of spinel stardust from the Murray meteorite. *The Astrophysical Journal* 717:107–120.

Hass K. C., Tamor M. A., Anthony T. R., and Banholzer W. F. 1992. Lattice dynamics and Raman spectra of isotopically mixed diamond. *Physical Review B* 45:7171–7182.

Heck P. R., Marhas K. K., Hoppe P., Gallino R., Baur H., and Wieler R. 2007. Presolar He and Ne isotopes in single

circumstellar SiC grains. *The Astrophysical Journal* 656:1208–1222.

Heck P. R., Jadhav M., Gyngard F., Busemann H., Maden C., and Wieler R. 2015. Presolar neon-22 in individual graphitic supernova spherules from Orgueil (abstract #5332). 78th Annual Meeting of the Meteoritical Society held in Berkeley, July 27–31, 2015.

Hoppe P., Annen P., Strebei R., Eberhardt P., Gallino R., Lugaro M., Amari S., and Lewis R. S. 1997. Meteoritic silicon carbide grains with unusual Si-isotopic compositions: Evidence from an origin in low-mass, low-metallicity asymptotic giant branch stars. *The Astrophysical Journal* 487:L101–L104.

Hoppe P., Strebel R., Eberhardt P., Amari S., and Lewis R. S. 2000. Isotopic properties of silicon carbide X grains from the Murchison meteorite in the size range 0.5−1.5 μm. *Meteoritics & Planetary Science* 35:1157–1176.

Hoppe P., Leitner J., Gröner E., Marhas K. K., Meyer B. S., and Amari S. 2010. NanoSIMS studies of small presolar SiC grains: New insights into supernova nucleosynthesis, chemistry, and dust formation. *The Astrophysical Journal* 719:1370–1384.

Huss G. R., Hutcheon I. D., and Wasserburg G. J. 1997. Isotopic systematics of presolar silicon carbide from the Orgueil (CI) chondrite: Implications for solar system formation and stellar nucleosynthesis. *Geochimica et Cosmochimica Acta* 61:5117–5148.

Hynes K. M., Croat T. K., Amari S., Mertz A. F., and Bernatowicz T. J. 2010. Structural and isotopic microanalysis of presolar SiC from supernovae. *Meteoritics & Planetary Science* 45:596–614.

Ivanov I. G., Yazdanfar M., Lundqvist B., Chen J.-T., Hassan J., Stenberg P., Liljedahl R., Son N. T., Ager III J. W., Kordina O., and Janzén E. 2014. High-resolution Raman and luminescence spectroscopy of isotope-pure $^{28}Si^{12}C$, natural and ^{13}C-enriched 4H-SiC. *Materials Science Forum* 778−780:471–474.

Kodolányi J., Vollmer C., Hoppe P., and Müller M. 2016. NanoSIMS and TEM investigations of supernova SiC grains (abstract #1478). 47th Lunar and Planetary Science Conference.

Li X.-B., Chen Z.-Z., and Shi E.-W. 2010. Effect of doping on the Raman scattering of 6H-SiC crystals. *Physica B* 405:2423–2426.

Lin Y., Gyngard F., and Zinner E. 2010. Isotopic analysis of supernova SiC and Si_3N_4 grains from the Qingzhen (EH3) chondrite. *The Astrophysical Journal* 709:1157–1173.

Lin S., Chen Z., Li L., and Yang C. 2012. Effect of impurities on the Raman scattering of 6H-SiC crystals. *Materials Research* 15:833–836.

Liu N., Savina M. R., Davis A. M., Gallino R., Straniero O., Gyndard F., Pellin M. J., Willingham D. G., Dauphas N., Piganatari M., Bisterzo S., Cristallo S., and Herwig F. 2014a. Barium isotopic composition of mainstream silicon carbides from Murchison: Constraints for *s*-process nucleosynthesis in asymptotic giant branch stars. *The Astrophysical Journal* 786:66–85.

Liu N., Gallino R., Bisterzo S., Davis A. M., Savina M. R., and Pellin M. J. 2014b. The ^{13}C-pocket structure in AGB models: Constraints from zirconium isotope abundances in single mainstream SiC grains. *The Astrophysical Journal* 788:163–169.

Liu N., Savina M. R., Gallino R., Davis A. M., Bisterzo S., Gyngard F., Käppeler F., Cristallo S., Dauphas N., Pellin M. J., and Dillmann I. 2015. Correlated strontium and barium isotopic compositions of acid-cleaned single mainstream silicon carbides from Murchison. *The Astrophysical Journal* 803:12–34.

Liu N., Nittler L. R., Alexander C. M. O'D., Wang J., Pignatari M., José J., and Nguyen A. 2016. Stellar origins of extremely ^{13}C- and ^{15}N-enriched presolar SiC grains: Novae or supernovae? *The Astrophysical Journal* 820:140–153.

Liu N., Nittler R. L., Pignatari M., Alexander M. O'D., and Wang J. 2017a. Stellar origin of ^{15}N-rich presolar SiC grains of type AB: Supernovae with explosive hydrogen burning. *The Astrophysical Journal Letters* 842:L1–L8.

Liu N., Stephan T., Boehnke P., Nittler L. R., Alexander C. M. O'D., Wang J., Davis A. M., Trappitsch R., and Pellin M. J. 2017b. J-type carbon stars: A dominant source of ^{14}N-rich presolar SiC grains of type AB. *The Astrophysical Journal Letters* 844:L12–L18.

Lugaro M., Davis A. M., Gallino R., and Pellin M. J. 2003. Isotopic compositions of strontium, zirconium, molybdenum, and barium in single presolar SiC grains and asymptotic giant branch stars. *The Astrophysical Journal* 593:486–508.

Marty B., Chaussidon M., Wiens R. C., Jurewicz A. J. G., and Burnett D. S. 2011. A ^{15}N-poor isotopic composition of the solar system as shown by Genesis solar wind samples. *Science* 332:1533–1536.

Nakashima S., and Harima H. 1997. Raman investigation of SiC polytypes. *Physica Status Solidi (a)* 162:39.

Nakashima S., Katahama H., Nakakura Y., and Mitsuishi A. 1986. Relative Raman intensities of the folded modes in SiC polytypes. *Physical Review B* 33:5721 (9 pp).

Nakashima S., Mitani T., Senzaki J., Okumura H., and Yamamoto T. 2005. Deep ultraviolet Raman scattering characterization of ion-implanted SiC crystals. *Journal of Applied Physics* 97:123,507 (8 pp).

Nicolussi G. K., Davis A. M., Pellin M. J., Lewis R. S., Clayton R. N., and Amari S. 1997. *s*-Process zirconium in presolar silicon carbide grains. *Science* 277:1281–1283.

Nicolussi G. K., Pellin M. J., Lewis R. S., Davis A. M., Clayton R. N., and Amari S. 1998a. Strontium isotopic composition in individual circumstellar silicon carbide grains: A record of *s*-process nucleosynthesis. *Physical Review Letters* 81:3583–3586.

Nicolussi G. K., Pellin M. J., Lewis R. S., Davis A. M., Amari S., and Clayton R. N. 1998b. Molybdenum isotopic composition of individual presolar silicon carbide grains from the Murchison meteorite. *Geochimica et Cosmochimica Acta* 62:1093–1104.

Nittler L. R. and Alexander C. M. O'D. 2003. Automated isotopic measurements of micron-sized dust: Application to meteoritic presolar silicon carbide. *Geochimica et Cosmochimica Acta* 67:4961–4980.

Nittler L. R., Amari S., Zinner E., Woosley S. E., and Lewis R. S. 1996. Extinct ^{44}Ti in presolar graphite and SiC: Proof of a supernova origin. *The Astrophysical Journal* 462:L31–L34.

Olego D. and Cardona M. 1982. Temperature dependence of the optical phonons and transverse effective charge in 3C-SiC. *Physical Review B* 25:3889–3896.

Pelletier M. J. 1999. Effects of temperature on cyclohexane Raman bands. *Applied Spectroscopy* 53:1087–1096.

Rohmfeld S., Hundhausen M., and Ley L. 1998. Raman scattering in polycrystalline 3C-SiC: Influence of stacking faults. *Physical Review B* 58:9858–9862.

Rohmfeld S., Hundhausen M., and Ley L. 2001. Isotope-disorder-induced line broadening of phonons in the Raman spectra of SiC. *Physical Review Letters* 86:826–829.

Savina M. R., Davis A. M., Tripa C. M., Pellin M. J., Clayton R. N., Lewis R. S., Amari S., Gallino R., and Lugaro M. 2003. Barium isotopes in individual presolar silicon carbide grains from the Murchison meteorite. *Geochimica et Cosmochimica Acta* 67:3201–3214.

Savina M. R., Davis A. M., Tripa C. E., Pellin M. J., Gallino R., Lewis R. S., and Amari S. 2004. Extinct technetium in silicon carbide stardust grains: Implications for stellar nucleosynthesis. *Science* 303:649–652.

Spitzer J., Etchegoin P., Cardona M., Anthony T. R., and Banholzer W. F. 1993. Isotopic-disorder induced Raman scattering in diamond. *Solid State Communications* 88:509–514.

Stroud R. M., Nittler L. R., and Hoppe P. 2004. Microstructures and isotopic compositions of two SiC X grains (abstract). *Meteoritics & Planetary Science* 39:A101.

Stroud R. M., Gyngard F., Nittler L. R., and Zinner E. K. 2015. Structural and chemical heterogeneity in the Bonanza supernova SiC grain (abstract # 1832). 46th Lunar and Planetary Science Conference.

Tseng C.-H., Ford J. F., Mann C. K., and Vickers I. J. 1993. Wavelength calibration of a multichannel spectrometer. *Applied Spectroscopy* 47:1808–1813.

Virag A., Wopenka B., Amari S., Zinner E., Anders E., and Lewis R. S. 1992. Isotopic, optical, and trace element properties of large single SiC grains from the Murchison meteorite. *Geochimica et Cosmochimica Acta* 56:1715–1733.

Wang D. T., Göbel A., Zegenhagen J., and Cardona M. 1997. Raman scattering on α-Sn: Dependence on isotopic composition. *Physical Review B* 56:13,167–13,171.

Wopenka B., Jadhav M., Lebsack E., and Zinner E. 2010. Raman and isotopic studies of large presolar SiC grains (abstract #1390). 41st Lunar and Planetary Science Conference. CD-ROM.

Zinner E. 2014. Presolar grains. In *Meteorites and cosmochemical processes*, edited by Holland H. D. and Turekian K. K. Treatise on Geochemistry, vol. 1. Oxford: Elsevier. pp. 181−210.

Zinner E., Ming T., and Anders E. 1987. Large isotopic anomalies of Si, C, N and noble gases in interstellar silicon carbide from the Murray meteorite. *Nature* 330:730–732.

Zinner E., Amari S., Guinness R., Nguyen A., Stadermann F. J., Walker R. M., and Lewis R. S. 2003. Presolar spinel grains from the Murray and Murchison carbonaceous chondrites. *Geochimica et Cosmochimica Acta* 67:5083–5095.

Zinner E., Nittler L. R., Gallino R., Karakas A. I., Lugaro M., Straniero O., and Lattanzio J. C. 2006. Silicon and carbon isotopic ratios in AGB stars: SiC grain data, models, and the galactic evolution of the Si isotopes. *The Astrophysical Journal* 650:350–373.

Zinner E., Amari S., Guinness R., Jennings C., Mertz A. F., Nguyen A. N., Gallino R., Hoppe P., Lugaro M., Nittler L. R., and Lewis R. S. 2007. NanoSIMS isotopic analysis of small presolar grains: Search for Si_3N_4 grains from AGB stars and Al and Ti isotopic compositions of rare presolar SiC grains. *Geochimica et Cosmochimica Acta* 71:4786–4813.

Zinner E., Jadhav M., Gyngard F., and Nittler L. R. 2011. Bonanza, a huge presolar SiC grain of type X (abstract #1070). 42nd Lunar and Planetary Science conference. CD-ROM.

SUPPORTING INFORMATION

Additional supporting information may be found in the online version of this article:

Table S1. NanoSIMS and EDX data of Mg-rich presolar SiC grains.

Table S2. NanoSIMS and Raman data of presolar SiC grains.

Data S1. M1-A7-G878 electron diffraction analysis summary for three patterns shown in Figs. 8D–F, respectively.